Sun, Z., Jian, Z., Stock, J.M., Larsen, H.C., Klaus, A., Alvarez Zarikian, C.A., and the Expedition 367/368 Scientists
Proceedings of the International Ocean Discovery Program Volume 367/368
publications.iodp.org

Data report: major and trace element and Nd-Pb-Hf isotope composition of the Site U1504 metamorphic basement in the South China Sea (IODP Expedition 367/368/368X)[1]

Susanne M. Straub,[2] Soumen Mallick,[3] Arturo Gomez-Tuena,[4] and Michael J. Dorais[5]

[1] Straub, S.M., Mallick, S., Gomez-Tuena, A., and Dorais, M.J., 2022. Data report: major and trace element and Nd-Pb-Hf isotope composition of the Site U1504 metamorphic basement in the South China Sea, IODP Expedition 367/368/368X. *In* Sun, Z., Jian, Z., Stock, J.M., Larsen, H.C., Klaus, A., Alvarez Zarikian, C.A., and the Expedition 367/368 Scientists, *South China Sea Rifted Margin*. Proceedings of the International Ocean Discovery Program, 367/368: College Station, TX (International Ocean Discovery Program). https://doi.org/10.14379/iodp.proc.367368.203.2022
[2] Lamont Doherty Earth Observatory, Columbia University, USA. **smstraub@ldeo.columbia.edu**
[3] Department of Earth, Environmental and Planetary Sciences, Brown University, USA.
[4] Centro de Geociencias, Universidad Nacional Autónoma de México, Mexico.
[5] Department of Geological Sciences, Brigham Young University, USA.

Contents

Keywords
International Ocean Discovery Program; IODP, *JOIDES Resolution*, Expedition 367, Expedition 368, South China Sea Rifted Margin, Site U1504

References (RIS)

MS 367368-203
Received 13 April 2021
Accepted 8 December 2021
Published 31 March 2022

Abstract

During International Ocean Discovery Program (IODP) Expedition 367/368/368X, Holes U1504A and U1504B were cored on the continental shelf (2817–2843 meters below sea level) in the northern South China Sea (SCS). A total of 106 m of metamorphic basement was penetrated that consists of greenish gray, deformed mylonitic, epidote-chlorite to calc-silicate schists containing granofels clasts ("greenschist"). Here we report bulk-rock major and trace element data from 17 greenschist samples, from which a subset of 9 samples was additionally analyzed for Pb-Nd-Hf isotope ratios. Fluid-mobile elements (U, Li, Rb, K, and Cs) behave somewhat erratically, yet tectonic discrimination and primitive mantle–normalized multielement diagrams reveal signatures that are typical for enriched intraplate basalts. These include a negative Pb anomaly (Ce/Pb = 34 ± 10), relative enrichments of Nb and Ta (Nb/La = 1.5 ± 0.3; Th/Nb = 0.07 ± 0.01), and a steep rare earth element pattern (La/Sm = 3.7 ± 0.7; Ho/Lu = 2.9 ± 0.2). The high values of the uranogenic $^{206}Pb/^{204}Pb$ (21.2–25.9) and $^{207}Pb/^{204}Pb$ (15.7–16.0) and their strong correlation point to a postformation "U addition event" that took place at 329 Ma ± 2 My (late Carboniferous). $^{143}Nd/^{144}Nd$ and $^{176}Hf/^{177}Hf$ data are consistent with the origin from an enriched Paleozoic age mantle source. In summary, our data suggest that the protolith of the Site U1504 metamorphic basement was an ocean-island basalt–type igneous rock that deformed during the late Paleozoic and was part of the prerift crustal basement of the SCS Basin.

1. Introduction

The key objectives of International Ocean Discovery Program (IODP) Expedition 367/368/368X were to (1) test scientific hypotheses of continental breakup at the northern South China Sea (SCS) margin in comparison to other nonvolcanic or magma-poor rifted margins and (2) further the knowledge of the Cenozoic paleoceanographic evolution of the SCS and Southeast Asia (**Larsen et al.**, 2018a). During Expedition 367/368/368X, the seven sites drilled across the northern SCS margin are located ~470 km south of the China mainland. Four sites (U1499, U1500, U1502, and U1503) are located in the continent–ocean transition (COT) in 3764–3868 m water depth, and three sites (U1501, U1504, and U1505) are located on the outer margin high (OMH) in 2816–2919 m water depth (Figure **F1**). Although the principal goal of the OMH sites was to obtain a record of the Neogene environmental evolution, information was also sought on the timing of

rifting, the rate of extension, and the degree of crustal exhumation through the recovery of prerift through synrift to postrift rock series (**Larsen et al.**, 2018a).

OMH Site U1504 (18°50.92′N, 116°14.54′E; 2816.6 meters below sea level [mbsl]) is located near the top of a structural high that appears to be the easterly extension of the much broader OMH section ~50 km to the west that was drilled at Site U1501 (**Larsen et al.**, 2018a). The acoustic basement at Site U1501 was reached at ~600 meters below seafloor (mbsf) and consists of highly lithified sandstones and conglomerate of likely Mesozoic age (**Larsen et al.**, 2018a). In contrast, the structural high is much narrower at Site U1504 and bounded by faults north (landward) and south (seaward) of the site. To the south, the top of the basement rapidly deepens (**Larsen et al.**, 2018b).

Site U1504 was only occupied because a flawed drawworks limited drilling operations during the second half of Expedition 368 to <3400 m water depth, which prevented further drilling in the COT (**Larsen et al.**, 2018b). Site U1504 was primarily targeted for the possibility of penetrating the acoustic basement under comparatively thin (~135 m) sediments and determining the nature and age of the basement (extrusive, intrusive, or metamorphic?) and the depth of lithospheric exposure by the tectonic exhumation.

After drilling through the ~135 m thick cover of late Eocene(?) to early Miocene to Pleistocene pelagic sediments, a total of 106 m of metamorphic basement was penetrated. The basement rocks are deformed epidote-chlorite-quartz schists, which are composed of a schistose, finer grained matrix with common centimeter- to decimeter-sized clasts of granofels, and subordinate epidote-chlorite gneiss clasts. These rocks were either referred to as “greenschists” because of their dominant green-gray color and alleged metamorphic facies or as “mylonites” because of the pervasive, fine-grained recrystallization and schistose deformation.

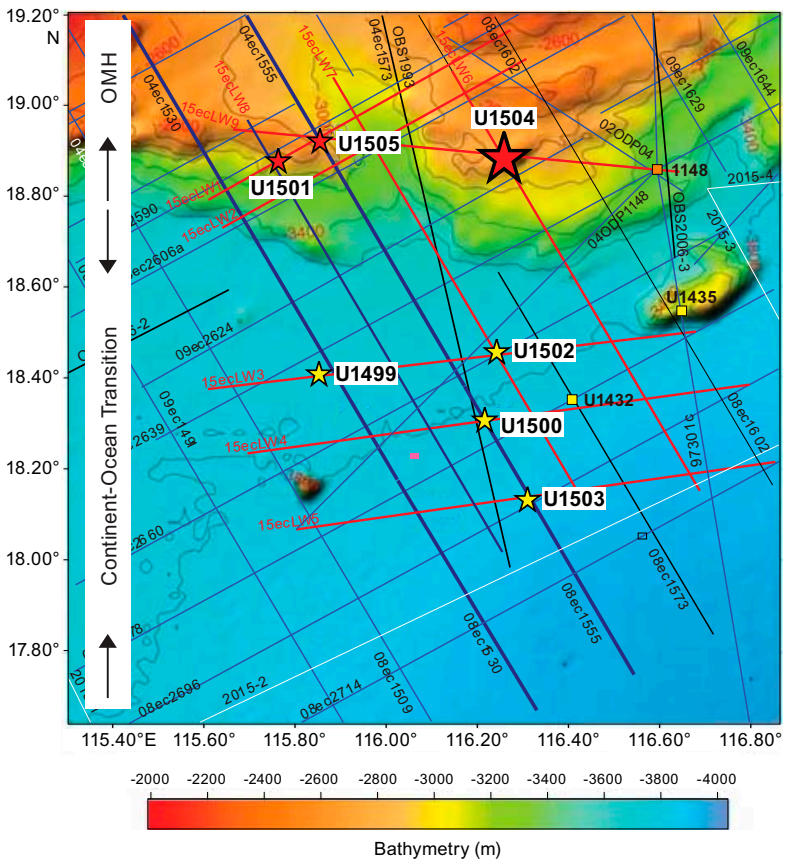

Figure F1. Site map, northern continental margin of South China Sea (modified from Larsen et al., 2018a). Red stars = Expedition 368 sites on OMH, yellow stars = Expedition 367/368/368X sites in COT, squares = Ocean Drilling Program Leg 184 and Expedition 349 sites.

Shipboard analyses comprised visual core descriptions (VCD), descriptive analyses of petrographic thin sections, X-ray diffraction (XRD) data, and preliminary bulk compositional data by handheld portable X-ray fluorescence spectrometer (pXRF) (**Larsen et al.**, 2018b). The preliminary data suggested that the protolith may have been a mafic, igneous rock with a composition more enriched than mid-ocean-ridge basalt (MORB) (**Larsen et al.**, 2018b). Additionally, the different clast sizes and deformation styles observed seemed to point toward a breccia as the protolith, which may have been a volcaniclastic rock or may have consisted of volcaniclasts that were embedded in a nonvolcanic or partially volcanic sedimentary matrix. Other possibilities discussed include a hydrothermally altered basalt, a metamorphosed basalt, metamorphosed continental crust, a fluid-cemented hydrothermal breccia matrix, a layered gabbro, or an ultramafic protolith (**Larsen et al.**, 2018b). Because the foliated mylonites are overlain by undeformed Eocene sediments at Site U1504, their metamorphism must be Eocene or older (**Larsen et al.**, 2018b). However, it remained uncertain whether the metamorphism has a relation to the Cenozoic continental rifting or these are older (Mesozoic to Paleozoic?) rocks that were part of the prerift continental crust (**Larsen et al.**, 2018b).

Here we report comprehensive major and trace element data of 17 samples, with a subset of 9 samples that were also analyzed for Nd-Pb-Hf isotope ratios. Although the goal was to better identify the protolith of the Site U1504 greenschists, the Pb isotope data unexpectedly provided an isochron age.

2. Geological setting

2.1. Geological setting of the South China Sea

The geology and evolution of the SCS has been described in detail elsewhere (e.g., **Larsen et al.**, 2018a; Sun, 2016; Yan et al., 2014). In short, the SCS is a marginal basin southwest of the South China block that formed during the Cenozoic by rifting and spreading of the pre-Cenozoic continental lithosphere along the eastern boundary of the Eurasian plate (Sun, 2016). The SCS rifting started in the late Paleogene and likely continued in the Eocene and early Oligocene (Sun, 2016). At around 30–31 Ma (early Oligocene), rifting was followed by seafloor spreading that lasted until ~15 Ma (**Larsen et al.**, 2018a). MORB-type oceanic crust was drilled at multiple locations (Expedition 349 Scientists, 2014; Zhang et al., 2017, 2018). Oceanic basin volcanism continued after the cessation of spreading in the form of younger late Miocene–Pliocene intraplate volcanoes ("young SCS seamounts") that erupted through the oceanic lithosphere (Tu et al., 1992; Yan et al., 2008, 2019; Zhang et al., 2017). Since ~15 Ma, the eastern SCS oceanic crust is subducted along the Manila Trench beneath the Luzon arc.

Knowledge of the composition and age of the prerift basement of the SCS is incomplete. There is agreement that prior to the SCS Basin formation the southeastern margin of the Eurasian South China block was an Andean-type subduction zone (e.g., Yan et al., 2010, 2011). This Mesozoic subduction zone produced granitic intrusive rocks that are dispersed across the SCS in the form of microblocks (Zhongsha, Xisha, Reed Bank, and Nansha) and are present at both the northern and southern continental margins (e.g., Yan et al., 2010, 2011). In addition, there is sparse evidence for older metamorphic basement rocks of early Mesozoic and Paleozoic age either from schists and quartzites that were drilled offshore in the Pearl River Mouth Basin (Zhou and Yao, 2009) or from upper Paleozoic to lower Mesozoic metamorphic rocks that are present on the conjugate southern continental margin on the Palawan Island in the Philippines (e.g., Suggate et al., 2014).

2.2. Site U1504 drilling and lithostratigraphy

At Site U1504, Holes U1504A and U1504B were drilled ~200 m apart with the rotary core barrel (RCB) system. In Hole U1504A (18°50.9199′N, 116°14.5397′E; 2816.6 mbsl), metamorphic basement was reached at 136.4 mbsf. A total of 27.35 m of greenschist was cored with a 19% recovery rate to 163.75 mbsf. Southeast in Hole U1504B (18°50.8213′N, 116°14.5978′E; 2843.0 mbsl), metamorphic basement was reached at 117.40 mbsf. A total of 78.88 m of greenschist was cored with a 21% recovery rate to 196.28 mbsf.

The basement was described as "metamorphic lithologic Unit 1," which consists of mylonitic, greenschist facies metamorphic rocks. The dominant lithology is epidote-chlorite to calc-silicate schists that contain centimeter- to decimeter-sized clasts of homogeneous, fine-grained granofels that are often crosscut by a network of quartz veins. Mylonitic foliation is strong in the schists, whereas the clasts show mostly isotropic textures with a locally developed weak foliation. Other lithologic variations include epidote-chlorite schist with granofels clasts, epidote-chlorite breccia, calc-silicate schist with granofels clasts, chlorite granofels, epidote granofels, epidote-chlorite granofels, chlorite schist with epidote, epidote-chlorite gneiss clasts, and rare, impure marble. The mineral assemblage in the schist and the granofels clasts is generally comparable and dominated by epidote, chlorite, plagioclase feldspar (albite?), and quartz. Traces of carbonate, illite-montmorillonite, smectite, dolomite, mica, and possibly pyroxenes were also reported (**Larsen et al.**, 2018b).

Although the principal lithology and mineralogy remains much the same, two metamorphic subunits were proposed based on the observed overall lithologic change and the compositional variation with increasing depth and between the two holes (**Larsen et al.**, 2018b). Metamorphic lithologic Subunit 1a comprises all of Hole U1504A (136.4–163.75 mbsf) and the upper part of Hole U1504B (117.40–141.72 mbsf). Subunit 1b comprises the lower part of Hole U1504B (141.72–196.28 mbsf). There are no clear-cut changes, and the principal differences between the two subunits lies in the higher abundance of veined gray granofels clasts in Subunit 1a relative to the overall higher abundance of lithologically more varied clasts and an overall increase in lithologic variety in deeper Subunit 1b. Moreover, in Subunit 1b the schistose matrix is more distinctly reddish brown, which was attributed to alteration. The lithologic downhole trend is accompanied by subtle compositional downhole variations (**Larsen et al.**, 2018b), the cause of which remains uncertain and may have either primary (inherent to protolith) or secondary (metamorphic overprint or alteration) causes.

3. Methods and materials

3.1. Sample selection and preparation

A total of 17 samples of metamorphic basement were taken from Hole U1504A (137.6–153.6 mbsf) and U1504B (119.0–187.6 mbsf) cores. A total of 10 samples (7 from Hole U1504A; 3 from Hole U1504B) are from metamorphic lithologic Subunit 1a, and 7 samples are from Subunit 1b. The samples are evenly distributed over the drill cores. They consist of fragments several centimeters in size that were leftovers from the surrounding 1 inch diameter mini drill cores that were taken for kinematic studies. No correlation with petrographic features was undertaken, yet based on visual inspection, the samples represent the lithologic variety of the metamorphic basement.

Any saw marks were removed from the rock fragments with sanding paper prior to reducing the fragments to smaller chips by crushing them between two plates of tempered steel. Clean-looking rock chips from the sieved 2–4 mm size fraction were then handpicked and washed in triple distilled water and methanol prior to powdering in an alumina mortar and pestle for major and trace element and isotope analyses.

3.2. Major and trace elements

All 17 samples were analyzed for major and trace elements (Table **T1**). Bulk-rock major element oxide analyses were done by X-ray fluorescence (XRF) analysis with a Rigaku ZSX Primus II at Brigham Young University (Provo, Utah). Bulk-rock trace element concentrations were determined by inductively coupled plasma–mass spectrometry (ICP-MS) using a Thermo iCap-Qc at UNAM Centro de Geociencias and following methods previously described by Mori et al. (2007), Gómez-Tuena et al. (2011), and Straub et al. (2015). To ensure dissolution of any refractory phases (e.g., zircon and oxides), all samples were digested in high pressure Parr bombs. A precise amount

Table T1. Major element oxide and trace element concentrations, Site U1504 metamorphic basement. **Download table in CSV format.**

of 50 ± 1 mg of sample powder was weighted in 15 mL polytetrafluoroethylene (PTFE) vials, digested overnight in a mixture of 1 mL of hydrofluoric acid (HF) and 0.5 mL of 8 M HNO_3 at 90°C, and then evaporated to almost dryness. Samples were transferred to 1.5 mL PTFE vials with 1 mL of HF and 0.5 mL of 8 M HNO_3 and then placed inside the PTFE liner of metal-jacketed Parr pressure bombs, to which 3 mL of a 2:1 HF-8 M HNO_3 mixture was added to equalize the pressure inside and outside the vials and prevent solution loss. The bombs were sealed and heated in an oven at 190°C for 5 days. After the bombs cooled to room temperature, the vials were removed, opened, and placed on a hot plate to evaporate the acids to almost dryness. To decompose any fluoride that might have formed in the previous steps, 1.5 mL of HCl was then added, and the vials were heated again in Parr bombs after adding 3 mL of 6 M HCl to the PTFE liner at 190°C in an oven for 24 h. After cooling, the samples were transferred to the original 15 mL vials and evaporated to dryness after fluxing the samples twice with 16 M of HNO_3. Finally, 2 mL of deionized water and 2 mL of 8 M HNO_3 were added to the samples and the closed vials were left overnight on a hot plate at 90°C.

For analysis, all samples were diluted by a factor of 2000. Samples were corrected for blanks and instrumental drift by internal standards (10 ppb Ge; 5 ppb of In, Tm, and Bi) and externally by a highly enriched alkali basalt that was repeatedly analyzed during the run (Sample PS-99-25 from the Palma Sola Massif [Gómez-Tuena et al., 2003]). Calibrations, based on international standards JB-2 (Geological Survey of Japan) and BHVO-2, BCR-2, and AGV-2 (U.S. Geological Survey), were strongly linear, and $R^2 \geq 0.999$ for most elements. For all elements, the precision (measured as 1 relative standard deviation of repeat samples) is usually better than 2%, as reported previously (Gómez-Tuena et al., 2011; Mori et al., 2007; Straub et al., 2015).

3.3. Pb-Hf-Nd isotope ratios of greenschists

Pb-Nd-Hf isotope ratios of a select subset of nine samples were analyzed with a Thermo Neptune+ MC-ICP mass spectrometer at Brown University (Providence, Rhode Island). Prior to digestion, the samples were treated to remove traces of seawater alteration. About 1 g of sample powders were leached with 6 M double distilled HCl for about 1 h on the hot plate at 100°C and then rinsed with 18 MΩ water three times. During each rinsing step, samples were centrifuged to ensure the complete removal of any residual acid. After drying the leached samples, about 100 mg of powder was dissolved in a 3:1 mixture of double distilled HF and HNO_3 mixture. Pb was separated first from the matrix using AG1-X8 (100–200 mesh, BIO-RAD) resin, followed by Hf using Ln resin (Eichrom) after Münker et al. (2001). The remaining matrix was passed through TRU-spec resin (Eichrom) to separate Rb-Sr from rare earth elements (REE), and the REE fraction was passed through Ln resin (Eichrom) to get a clean Nd fraction.

Nd, Hf, and Pb isotopic compositions were measured on a Thermo Scientific NEPTUNE PLUS MC-ICP-MS at the Mass Spectrometer Analytical Facility at Brown University (DeFelice et al., 2019; Yakovlev et al., 2019). Samples were introduced in the plasma using a perfluoroalkoxy (PFA) nebulizer with a flow rate of ~70 µL/min coupled with an APEX-IR introduction system to enhance the sensitivity. The mass spectrometer was equipped with an H-skimmer cone and H-sampler cone. The baseline measurement was taken at –0.5 amu. $^{143}Nd/^{144}Nd$ and $^{176}Hf/^{177}Hf$ were corrected for instrumental mass fractionation using $^{146}Nd/^{144}Nd = 0.7219$ and $^{179}Hf/^{177}Hf = 0.7325$, respectively, with an exponential law. Pb solution was spiked with NBS SRM-997 Tl standard prior to analysis with a Pb/Tl of 4 to correct for the mass fractionation using an exponential law with a $^{203}Tl/^{205}Tl$ of 0.418922. Nd and Hf were measured around 100 ppb concentration, whereas Pb was measured around 75 ppb concentration. The $^{143}Nd/^{144}Nd$ and $^{176}Hf/^{177}Hf$ of samples are reported relative to JNd-i Nd standard ($^{143}Nd/^{144}Nd = 0.512115$) and JMC-475 Hf standard ($^{176}Hf/^{177}Hf = 0.282160$), respectively. $^{206}Pb/^{204}Pb$, $^{207}Pb/^{204}Pb$, $^{208}Pb/^{204}Pb$ are reported relative to the NBS 981 standard ($^{206}Pb/^{204}Pb = 16.9356$, $^{207}Pb/^{204}Pb = 15.4891$, and $^{208}Pb/^{204}Pb = 36.7006$) (Todt et al., 1996). The external precision on the ratios over the course of several years is 30 ppm for Nd (2σ; $n = 104$), 40 ppm for Hf (2σ; $n = 89$), and 45–80 ppm for Pb (2σ; $n = 75$). Pb blanks were <50 pg, and Nd and Hf blanks were <30 pg.

Geochemical reference material BCR-2 was processed along with the samples and during the same run yielded values of 0.512640 ± 0.000006 (2σ; 12 ppm) for $^{143}Nd/^{144}Nd$, 0.282864 ± 0.000005

(2σ; 17 ppm) for $^{176}Hf/^{177}Hf$, 18.7580 ± 0.0006 (2σ; 31 ppm) for $^{206}Pb/^{204}Pb$, 15.6164 ± 0.0006 (2σ; 36 ppm) for $^{207}Pb/^{204}Pb$, and 38.7208 ± 0.0018 (2σ; 48 ppm) for $^{208}Pb/^{204}Pb$.

4. Results

4.1. Major and trace elements

4.1.1. General variations

Major element oxide and trace element data are presented in Table **T1**. The new XRF data confirm the shipboard assessment (**Larsen et al.**, 2018b) that the Site U1504 metamorphic basement resembles enriched oceanic basalts. In a total alkali (Na_2O + K_2O) versus SiO_2 classification diagram (not shown), the greenschists plot in the field of low silica (<50 wt%) alkali basalts, which are typically erupted from oceanic intraplate volcanoes. On the other hand and in view of the metamorphic overprint and high loss on ignition (LOI = 2.9–9.5; Table **T1**), loss or gain of key elements like FeO, MgO, K_2O, and Na_2O is likely, and thus a classification based on major element oxides remains tentative.

Alternatively, classification diagrams with alteration-resistant trace elements can be used. In two diagrams (Zr/Ti vs. Nb/Y and SiO_2 vs. Nb/Y; Figure **F2**) after Winchester and Floyd (1977), all samples, with one exception, plot in the field of alkaline basalts. The affinity to intraplate basalts also shows in the Hf/3–Th–Ta diagram after Wood (1980) (Figure **F3A**) and the Ti/100–Zr–Y × 3 tectonic discrimination diagram after Pearce and Cann (1973) (Figure **F3B**).

Incompatible trace element patterns are also consistent with this classification. In Figure **F4**, multielement diagrams on the left side display all incompatible trace elements, including those that are sensitive to fluid-induced mobilization during alteration or metamorphosis (e.g., Li, U, Cs, Rb, and K). The multielement diagrams on the right side display selected trace elements that are resistant to fluid mobilization (e.g., Th, Nb, Ta, Y, and REE). In either case, and despite the somewhat erratic behavior of the fluid-mobile elements, the greenschists display the typical trace ele-

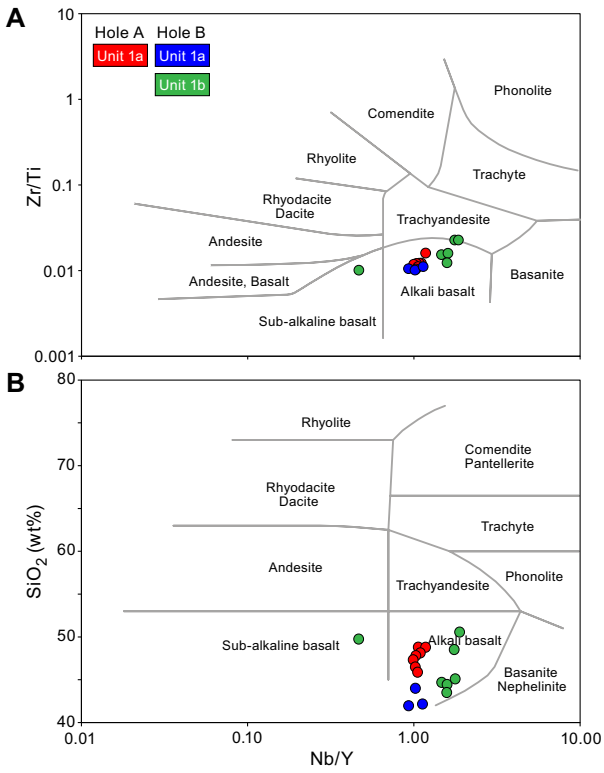

Figure F2. A, B. Whole-rock classification diagrams after Winchester and Floyd (1977).

ment signature of enriched intraplate basalts. For example, there is the typical, prominent negative Pb anomaly and high Ce/Pb (34 ± 10) of mantle-normalized ocean-island basalt (OIB)-type rocks. Other characteristics are the relative depletions that for K and Rb are at least partially visible, despite their increased variability, which is likely due to a postformation overprint. The greenschists have the OIB-type relative enrichments of Nb and Ta and thus the typical high Nb/La (1.5 ± 0.3) and low Th/Nb (0.07 ± 0.01), as well as the typical steep REE patterns with high La/Sm (3.7 ± 0.7) and Ho/Lu (2.9 ± 0.2) that are distinct from the low La/Sm (1.2) and Ho/Lu (2.5) of MORB-type magmas (Gale et al., 2013). The latter feature clearly sets apart the greenschists from the Cenozoic MORB-type SCS basalts drilled at IODP Expedition 349 Site U1431 in the central SCS Basin, which also have low MORB-type La/Sm (1.0 ± 0.3) and Ho/Lu (2.4 ± 0.1) (Zhang et al., 2017, 2018).

Although the greenschists resemble OIB-type magmas, they are not as enriched as other intraplate magmas. For example, in comparison to typical OIB-type island basalts the greenschists have lower and shallower light REE abundances and also more moderate ratios of middle to heavy REE (e.g., greenschist Ho/Lu = 2.9 ± 0.2 compared to Ho/Lu >3.5 in intraplate magmas [Willbold and Stracke, 2006]). Likewise, the Miocene intraplate alkali basalts that erupted at Site U1431 after the termination of the seafloor spreading have higher Ho/Lu (3.4 ± 0.3). However, the greenschists overlap in Ho/Lu with the younger Miocene–Pliocene seamounts in the SCS (Ho/Lu = 2.8 ± 0.2), even though the latter are still more enriched in light REE than the greenschists.

4.1.2. Downhole variations

Downhole trends of selected incompatible trace elements and ratios are shown in Figure **F5**. A multielement diagram of the different subunits is shown in Figure **F6**. Clearly, the abundance of the highly incompatible elements (left side of Figure **F6**) increase downhole by roughly a factor of 2–3. However, the ratios of fluid-immobile incompatible trace elements remain constant (e.g., Ho/Lu, Zr/Nb, Th/Nb, La/Sm, and Nb/Ta). This suggests that the presumed OIB-type protolith may have been composed of several units with different levels of enrichment but that are cogenetic

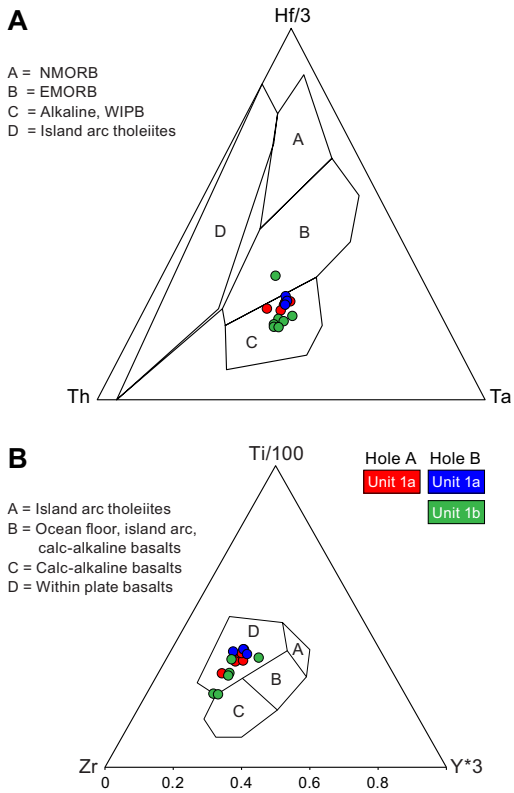

Figure F3. Tectonic discrimination diagrams. A. After Wood (1980). NMORB = normal MORB, EMORB = enriched MORB, WIPB = within plate basalt. B. After Pearce and Cann (1973).

all the same. Element abundances in cogenetic igneous series can vary due to variable extents of melting or fractional crystallization.

Although the trends of the fluid-immobile element are robust, elements sensitive to fluid mobilization are more erratic and can be decoupled from the trends of the fluid-immobile elements and, in addition, can be decoupled from each other. For example, although U/Nb displays maxima in some samples from deeper Subunit 1b, Li/Y reaches maxima in Subunit 1a, whereas Rb/Nb is largely indifferent. These erratic variations may have been caused by alteration or the metamorphic overprinting, which may have taken place in more than a single event.

4.2. Pb isotope ratios and Pb isochron ages

The measured Pb isotope ratios of the greenschists are very high ($^{206}Pb/^{204}Pb$ = 21.23–25.90, $^{207}Pb/^{204}Pb$ = 15.71–15.96, and $^{208}Pb/^{204}Pb$ = 40.73–41.87; Table **T2**) and plot in their entirety outside the field of modern and ancient OIB-type and MORB-type volcanic rocks (Figure **F7**). The high Pb isotope ratios point to substantial postformation ingrowth of the radiogenic daughter Pb isotopes (^{206}Pb, ^{207}Pb, and ^{208}Pb), which could have been augmented by secondary selective enrichment(s) of U and/or Th relative to Pb.

The excellent positive correlation between two uranogenic Pb isotope ratios, $^{206}Pb/^{204}Pb$ and $^{207}Pb/^{204}Pb$ (R^2 = 0.9999; n = 9), and their lack of correlation with the thorogenic $^{208}Pb/^{204}Pb$ point

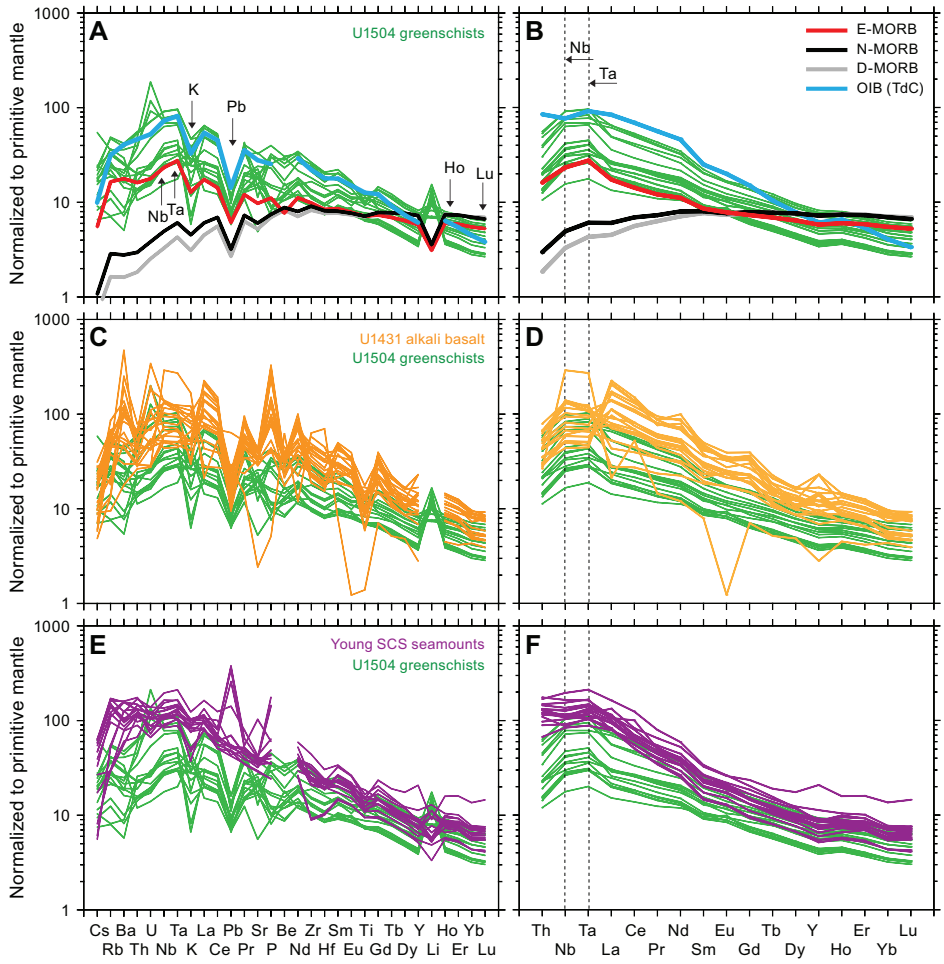

Figure F4. Multielement trace element diagrams of Site U1504 greenschists normalized to primitive mantle (McDonough and Sun, 1995) compared to (A, B) average depleted (D), normal (N), and enriched (E) MORB (Gale et al., 2013) and OIB-type oceanic basalts exemplified by Tristan da Cunha (TdC; Willbold and Stracke, 2006); (C, D) postspreading Miocene intraplate alkali basalts from Site U1431 (Zhang et al., 2017, 2018); and (D, E) Miocene–Pliocene young SCS seamounts (Yan et al., 2008).

to a single "U enrichment event," during which the fluid-mobile U (with ^{238}U and ^{235}U producing radiogenic ^{206}Pb and ^{207}Pb, respectively) was added to the rock. In contrast, the fluid-immobile ^{232}Th (producing radiogenic ^{208}Pb) was either not affected or at least far less mobilized than U. Selective U addition can be effected by seawater alteration (Hauff et al., 2003), but U could also be added during fluid-present metamorphism/deformation. It is noteworthy that all samples with very high $^{206}Pb/^{204}Pb$ and $^{207}Pb/^{204}Pb$ are from metamorphic lithologic Subunit 1b in the deeper part of the drilled metamorphic basement (Figure **F8**). However, one sample from Subunit 1b has similar low Pb isotopes to samples from Subunit 1a, suggesting that not all parts of Subunit 1b were equally affected by a selective U addition.

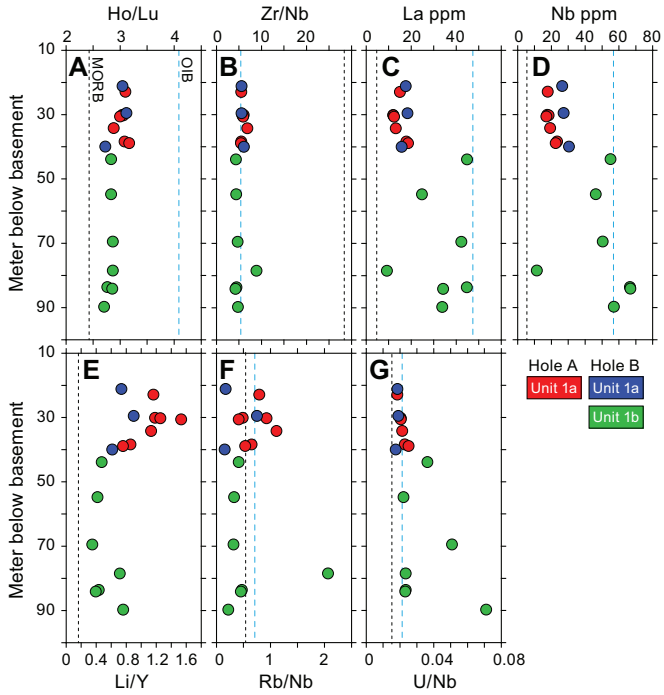

Figure F5. A–G. Downhole trends (starting at top of Holes U1504A and U1504B) of select incompatible trace elements and trace element ratios in Site U1504 metamorphic basement. Average MORB from Gale et al. (2013). OIB exemplified by Tristan da Cunha average from Willbold and Stracke (2006).

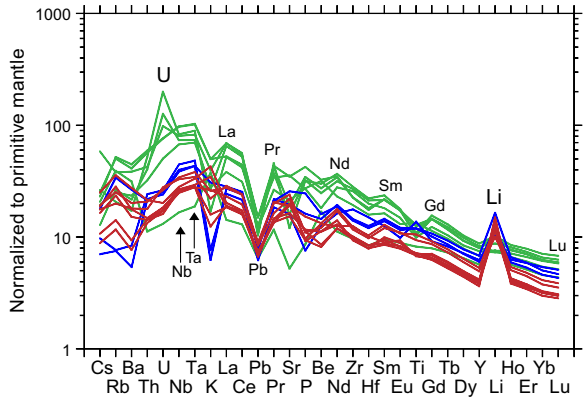

Figure F6. Multielement trace element diagram of greenschists normalized to primitive mantle from McDonough and Sun (1995), Subunit 1a in Holes U1504A (red) and U1504B (blue) and Subunit 1b in Hole U1504B (green).

Table T2. Measured and initial Pb isotope ratios, Site U1504 metamorphic basement. **Download table in CSV format.**

Treating the regression line in the uranogenic Pb isotope diagram as an isochron allows for calculating a "bulk-rock" Pb age. Pb-Pb ages were calculated with the IsoplotR software package (Vermeesch, 2018) using a maximum likelihood regression, yielding an isochron age of 329 ± 2 Ma, which falls in the middle of the Carboniferous period of the Paleozoic era. The inverse Pb-Pb iso-

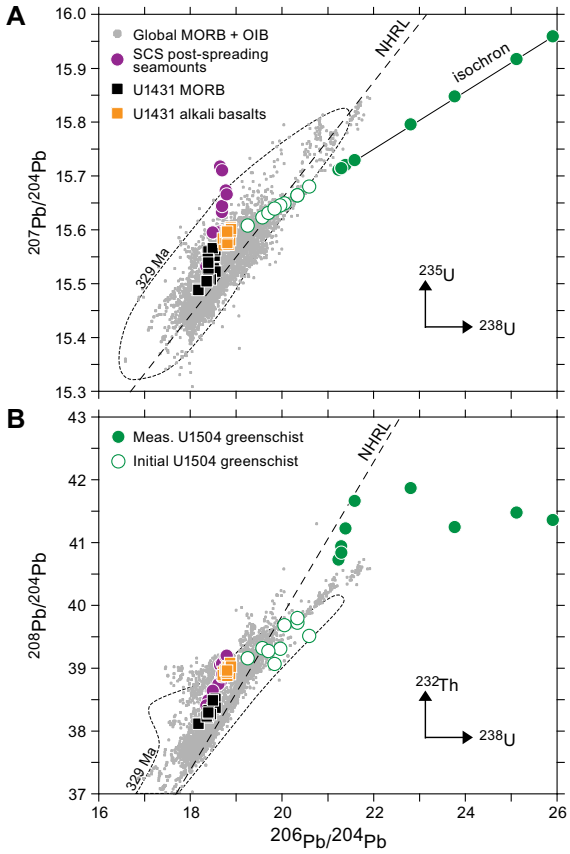

Figure F7. (A) $^{206}Pb/^{204}Pb$ vs. $^{207}Pb/^{204}Pb$ and (B) $^{206}Pb/^{204}Pb$ vs. $^{208}Pb/^{204}Pb$ of Site U1504 greenschists compared to global MORB and OIB (Willbold and Stracke, 2010), MORB-type Miocene basalts and younger alkaline basalts from Site U1431 in the SCS (Zhang et al., 2017, 2018), and Miocene–Pliocene young SCS seamounts (Yan et al., 2008). NHRL = Northern Hemisphere reference line (Dupré and Allègre, 1983). MORB/OIB at 329 Ma (dashed area) calculated with U, Th, and Pb abundances for average depleted MORB mantle from Workman and Hart (2005) for MORB and for primitive mantle from McDonough and Sun (1995) for OIB. Arrows = direction of ingrowth from radioactive ^{235}U (^{207}Pb), ^{238}U (^{206}Pb), and ^{232}Th (^{208}Pb).

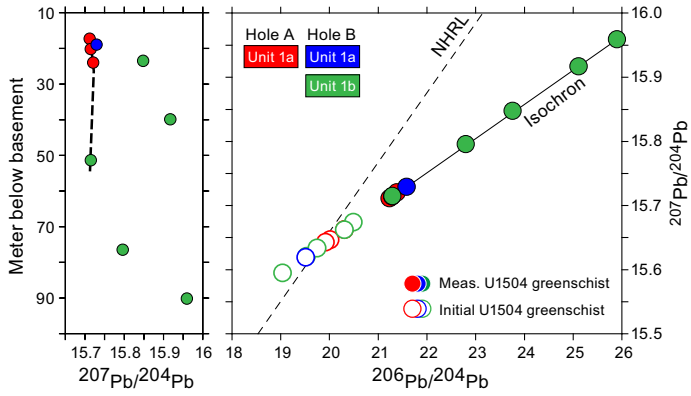

Figure F8. Pb isotope variations in metamorphic subunits, Site U1504 greenschists. Left: Downhole variation of $^{207}Pb/^{204}Pb$. Right: $^{206}Pb/^{204}Pb$ vs. $^{207}Pb/^{204}Pb$ for measured and initial Pb isotope ratios calculated with age of 329 ± 2 Ma. NHRL = Northern Hemisphere reference line.

chron on the measured Pb isotope ratios (Figure **F9**) is associated with a mean squared weighted deviates (MSWD) of 11 (and thus >1) and a p-value of the chi-square test ($p[\chi^2]$) of ≪0.05. These two parameters indicate that ages are overdispersed with respect to the stated analytical uncertainty. This implies that either the system was not entirely at equilibrium at the time of the U addition event or that the system was not fully closed since then. A geological dispersion is not surprising, given that the isochron data are from nine samples that are distributed over a 67 m thick rock sequence that is not entirely homogeneous (Figure **F8**). However, the influence of the geological dispersion on the calculated age seems small because the MSWD is not very much > 1. Moreover, other modes of calculations with IsoplotR (Vermeesch, 2018) that assume ab initio that the data dispersion exceeds the analytical uncertainty yield very similar isochron ages of 331 ± 8 Ma and 331 ± 10 Ma that entirely overlap with the age of 329 ± 2 Ma.

The U addition event must be equal to or younger than rock formation age, and thus it provides a minimum rock formation age. Calculation of the initial Pb isotope ratios of the greenschists (Figure **F8**; Table **T2**) using the Carboniferous age casts all initial Pb isotope ratios back into the mantle field of the Paleozoic area. Although this projection generally supports the calculated age (Carboniferous Pb isotope ratios of volcanic rocks must lie in the Carboniferous mantle field), they do not exclude that the rock formation age may be older by up to an additional 100 Ma.

4.3. Nd-Hf isotope ratios

Unlike the U-Th-Pb isotope system, in the ^{147}Sm-^{143}Nd and ^{176}Lu-^{176}Hf isotope systems, both radioactive parent and radiogenic daughter isotopes are resistant to mobilization during alteration and metamorphism. Therefore, low measured $^{143}Nd/^{144}Nd$ (0.511277–0.51288) and $^{176}Hf/^{177}Hf$ (0.28282–0.28291) isotope ratios (Table **T3**) are likely affected by age-related ingrowth only. Measured $^{143}Nd/^{144}Nd$ and $^{176}Hf/^{177}Hf$ plot just within the array of modern oceanic basalts (Figure **F10**) and do not overlap with Cenozoic SCS oceanic basalts. Thus, the greenschist protolith and the Cenozoic SCS oceanic basalts must have originated from two different mantle sources.

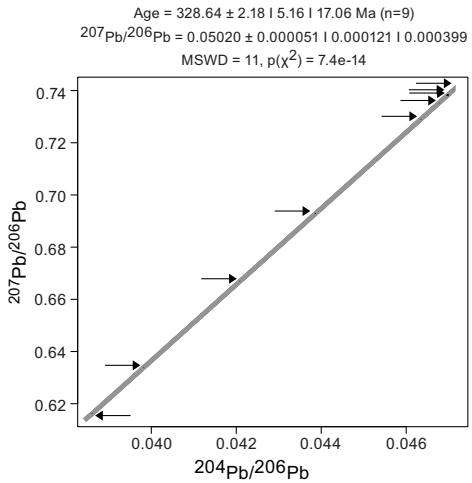

Figure F9. Inverse $^{206}Pb/^{204}Pb$ vs. $^{207}Pb/^{204}Pb$ diagram from IsoplotR (Vermeesch, 2018), Site U1504. Black arrows point to sample (small black dots; errors are too small to be visible) on isochron line. Calculation uses analytical uncertainty of 2 standard error (SE) abs, error correlation (ρ) of $^{206}Pb/^{204}Pb$ and $^{207}Pb/^{204}Pb$ (Ludwig, 1988), $^{238}U/^{235}U$ = 137.818 ± 0.0225, ^{238}U decay constant = 0.000155125 ± 0.000000083, and ^{235}U decay constant = 0.00098485 ± 0.00000067. Line 1: Isochron age and its estimated uncertainty (σ), studentized 100(1-α)% confidence interval for isochron age using appropriate number of degrees of freedom, and approximate 100(1 − α)% confidence interval for isochron age with overdispersion, calculated as $z = y\sqrt{\text{MSWD}}$. Line 2: Initial $^{207}Pb/^{204}Pb$ obtained by linear regression and its estimated uncertainty (σ), studentized 100(1 − α)% confidence interval for initial $^{207}Pb/^{204}Pb$ using appropriate number of degrees of freedom, approximate 100(1 − α)% confidence interval for initial $^{207}Pb/^{204}Pb$ with overdispersion, calculated as $z = y\sqrt{\text{MSWD}}$. Line 3: MSWD for linear fit, chi-square p-value ($p[\chi^2]$) for the fit (0.000000000000074).

Table T3. Measured and initial Nd and Hf isotope ratios, Site U1504 metamorphic basement. **Download table in CSV format.**

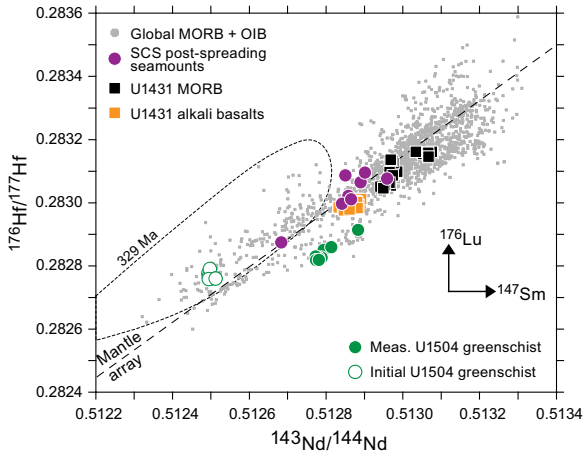

Figure F10. $^{176}Hf/^{177}Hf$ vs. $^{143}Nd/^{144}Nd$ of Site U1504 greenschists compared to global MORB (Gale et al., 2013) and OIB (Willbold and Stracke, 2010), MORB-type Miocene basalts and younger alkaline basalts from Site U1431 in the SCS (Zhang et al., 2017, 2018), and Miocene–Pliocene young SCS seamounts (Yan et al., 2008, 2019). Mantle array after Vervoort et al. (1999). MORB/OIB at 329 Ma (dashed area) calculated with Sm, Nd, Lu and Hf abundances for average depleted MORB mantle from Workman and Hart (2005) for MORB, and for primitive mantle from McDonough and Sun (1995) for OIB. Pictogram-arrows indicating direction of ingrowth from radioactive ^{147}Sm (^{143}Nd) and ^{176}Lu (^{176}Hf).

After correction for age-related ingrowth using the Carboniferous age of 329 Ma, the initial $^{143}Nd/^{144}Nd_i$ and $^{176}Hf/^{177}Hf_i$ of the greenschists still plot within the field of age-corrected oceanic basalts. The increase in the deviation from chondritic uniform reservoir (CHUR) from the measured εNd = +3.1 and εHf = +1.7 values to initial εNd_{in} = +5.5 and εHf_{in} = +6.9, respectively, are also consistent with the origin from depleted Carboniferous mantle sources (Table **T3**). In summary, the age-corrected $^{143}Nd/^{144}Nd$ and $^{176}Hf/^{177}Hf$ of the greenschists are consistent with the Paleozoic minimum rock formation age of 329 ± 2 Ma, although they do not constrain an absolute age.

5. Acknowledgments

This research used samples and data provided by the International Ocean Discovery Program (IODP). Funding for this research was provided by an USSSP Post Expedition Activity Award Grants to S.M. Straub and M.J. Dorais. Irina Liu (Lamont) and Ofelia Perez-Arfizu (UNAM Centro de Geociencias) are thanked for their assistance with sample preparation and analysis.

References

Bouvier, A., Vervoort, J.D., and Patchett, P.J., 2008. The Lu–Hf and Sm–Nd isotopic composition of CHUR: constraints from unequilibrated chondrites and implications for the bulk composition of terrestrial planets. Earth and Planetary Science Letters, 273(1):48–57. **https://doi.org/10.1016/j.epsl.2008.06.010**

DeFelice, C., Mallick, S., Saal, A.E., and Huang, S., 2019. An isotopically depleted lower mantle component is intrinsic to the Hawaiian mantle plume. Nature Geoscience, 12(6):487–492. **https://doi.org/10.1038/s41561-019-0348-0**

Dupré, B., and Allègre, C.J., 1983. Pb–Sr isotope variation in Indian Ocean basalts and mixing phenomena. Nature, 303(5913):142–146. **https://doi.org/10.1038/303142a0**

Expedition 349 Scientists, 2014. South China Sea tectonics: opening of the South China Sea and its implications for southeast Asian tectonics, climates, and deep mantle processes since the late Mesozoic. International Ocean Discovery Program Preliminary Report, 349. **https://doi.org/10.14379/iodp.pr.349.2014**

Gale, A., Dalton, C.A., Langmuir, C.H., Su, Y., and Schilling, J.-G., 2013. The mean composition of ocean ridge basalts. Geochemistry, Geophysics, Geosystems, 14(3):489–518. **https://doi.org/10.1029/2012GC004334**

Gómez-Tuena, A., LaGatta, A.B., Langmuir, C.H., Goldstein, S.L., Ortega-Gutiérrez, F., and Carrasco-Núñez, G., 2003. Temporal control of subduction magmatism in the eastern Trans-Mexican Volcanic Belt: mantle sources, slab contributions, and crustal contamination. Geochemistry, Geophysics, Geosystems, 4(8):8912. **https://doi.org/10.1029/2003GC000524**

Gómez-Tuena, A., Mori, L., Goldstein, S.L., and Pérez-Arvizu, O., 2011. Magmatic diversity of western Mexico as a function of metamorphic transformations in the subducted oceanic plate. Geochimica et Cosmochimica Acta, 75(1):213–241. **https://doi.org/10.1016/j.gca.2010.09.029**

Hauff, F., Hoernle, K., and Schmidt, A., 2003. Sr-Nd-Pb composition of Mesozoic Pacific oceanic crust (Site 1149 and 801, ODP Leg 185): implications for alteration of ocean crust and the input into the Izu-Bonin-Mariana subduction system. Geochemistry, Geophysics, Geosystems, 4(8):8913. **https://doi.org/10.1029/2002GC000421**

Larsen, H.C., Sun, Z., Stock, J.M., Jian, Z., Alvarez Zarikian, C.A., Klaus, A., Boaga, J., Bowden, S.A., Briais, A., Chen, Y., Cukur, D., Dadd, K.A., Ding, W., Dorais, M.J., Ferré, E.C., Ferreira, F., Furusawa, A., Gewecke, A.J., Hinojosa, J.L., Höfig, T.W., Hsiung, K.-H., Huang, B., Huang, E., Huang, X.-L., Jiang, S., Jin, H., Johnson, B.G., Kurzawski, R.M., Lei, C., Li, B., Li, L., Li, Y., Lin, J., Liu, C., Liu, C., Liu, Z., Luna, A., Lupi, C., McCarthy, A.J., Mohn, G., Ningthoujam, L.S., Nirrengarten, M., Osono, N., Peate, D.W., Persaud, P., Qiu, N., Robinson, C.M., Satolli, S., Sauermilch, I., Schindlbeck, J.C., Skinner, S.M., Straub, S.M., Su, X., Tian, L., van der Zwan, F.M., Wan, S., Wu, H., Xiang, R., Yadav, R., Yi, L., Zhang, C., Zhang, J., Zhang, Y., Zhao, N., Zhong, G., and Zhong, L., 2018a. Expedition 367/368 summary. In Sun, Z., Jian, Z., Stock, J.M., Larsen, H.C., Klaus, A., Alvarez Zarikian, C.A., and the Expedition 367/368 Scientists, South China Sea Rifted Margin. Proceedings of the International Ocean Discovery Program, 367: College Station, TX (International Ocean Discovery Program). **https://doi.org/10.14379/iodp.proc.367368.101.2018**

Larsen, H.C., Jian, Z., Alvarez Zarikian, C.A., Sun, Z., Stock, J.M., Klaus, A., Boaga, J., Bowden, S.A., Briais, A., Chen, Y., Cukur, D., Dadd, K.A., Ding, W., Dorais, M.J., Ferré, E.C., Ferreira, F., Furusawa, A., Gewecke, A.J., Hinojosa, J.L., Höfig, T.W., Hsiung, K.-H., Huang, B., Huang, E., Huang, X.-L., Jiang, S., Jin, H., Johnson, B.G., Kurzawski, R.M., Lei, C., Li, B., Li, L., Li, Y., Lin, J., Liu, C., Liu, C., Liu, Z., Luna, A., Lupi, C., McCarthy, A.J., Mohn, G., Ningthoujam, L.S., Nirrengarten, M., Osono, N., Peate, D.W., Persaud, P., Qiu, N., Robinson, C.M., Satolli, S., Sauermilch, I., Schindlbeck, J.C., Skinner, S.M., Straub, S.M., Su, X., Tian, L., van der Zwan, F.M., Wan, S., Wu, H., Xiang, R., Yadav, R., Yi, L., Zhang, C., Zhang, J., Zhang, Y., Zhao, N., Zhong, G., and Zhong, L., 2018b. Site U1504. In Sun, Z., Jian, Z., Stock, J.M., Larsen, H.C., Klaus, A., Alvarez Zarikian, C.A., and the Expedition 367/368 Scientists, South China Sea Rifted Margin. Proceedings of the International Ocean Discovery Program, 367/368: College Station, TX (International Ocean Discovery Program). **https://doi.org/10.14379/iodp.proc.367368.108.2018**

Ludwig, K.R., 1988. ISOPLOT for MS-DOS, a plotting and regression program for radiogenic-isotope data, for IBM-PC compatible computers, version 1.00. Open-File Report, 88-557. **https://doi.org/10.3133/ofr88557**

McDonough, W.F., and Sun, S., 1995. The composition of the Earth. Chemical Geology, 120(3):223–253. **https://doi.org/10.1016/0009-2541(94)00140-4**

Mori, L., Gómez-Tuena, A., Cai, Y., and Goldstein, S.L., 2007. Effects of prolonged flat subduction on the Miocene magmatic record of the central Trans-Mexican Volcanic Belt. Chemical Geology, 244(3):452–473. **https://doi.org/10.1016/j.chemgeo.2007.07.002**

Münker, C., Weyer, S., Scherer, E., and Mezger, K., 2001. Separation of high field strength elements (Nb, Ta, Zr, Hf) and Lu from rock samples for MC-ICPMS measurements. Geochemistry, Geophysics, Geosystems, 2(12). **https://doi.org/10.1029/2001GC000183**

Pearce, J.A., and Cann, J.R., 1973. Tectonic setting of basic volcanic rocks determined using trace element analyses. Earth and Planetary Science Letters, 19(2):290–300. **https://doi.org/10.1016/0012-821X(73)90129-5**

Straub, S.M., Gómez-Tuena, A., Bindeman, I.N., Bolge, L.L., Brandl, P.A., Espinasa-Perena, R., Solari, L., Stuart, F.M., Vannucchi, P., and Zellmer, G.F., 2015. Crustal recycling by subduction erosion in the central Mexican Volcanic Belt. Geochimica et Cosmochimica Acta, 166:29–52. **https://doi.org/10.1016/j.gca.2015.06.001**

Suggate, S.M., Cottam, M.A., Hall, R., Sevastjanova, I., Forster, M.A., White, L.T., Armstrong, R.A., Carter, A., and Mojares, E., 2014. South China continental margin signature for sandstones and granites from Palawan, Philippines. Gondwana Research, 26(2):699–718. **https://doi.org/10.1016/j.gr.2013.07.006**

Sun, W., 2016. Initiation and evolution of the South China Sea: an overview. Acta Geochimica, 35(3):215–225. **https://doi.org/10.1007/s11631-016-0110-x**

Todt, W., Cliff, R.A., Hanser, A., and Hofmann, A.W., 1996. Evaluation of a ^{202}Pb–^{205}Pb double spike for high-precision lead isotope analysis. In Basu, A., and Hart, S. (Eds.), Earth Processes: Reading the Isotopic Code. Geophysical Monograph: 429–437. **https://doi.org/10.1029/GM095p0429**

Tu, K., Flower, M.F.J., Carlson, R.W., Xie, G., Chen, C.-Y., and Zhang, M., 1992. Magmatism in the South China Basin, 1. Isotopic and trace-element evidence for an endogenous Dupal mantle component. Chemical Geology, 97(1):47–63. **https://doi.org/10.1016/0009-2541(92)90135-R**

Vermeesch, P., 2018. IsoplotR: a free and open toolbox for geochronology. Geoscience Frontiers, 9(5):1479–1493. **https://doi.org/10.1016/j.gsf.2018.04.001**

Vervoort, J.D., Patchett, P.J., Blichert-Toft, J., and Albarède, F., 1999. Relationships between Lu–Hf and Sm–Nd isotopic systems in the global sedimentary system. Earth and Planetary Science Letters, 168(1):79–99. **https://doi.org/10.1016/S0012-821X(99)00047-3**

Willbold, M., and Stracke, A., 2006. Trace element composition of mantle end-members: implications for recycling of oceanic and upper and lower continental crust. Geochemistry, Geophysics, Geosystems, 7(4):Q04004. **https://doi.org/10.1029/2005GC001005**

Willbold, M., and Stracke, A., 2010. Formation of enriched mantle components by recycling of upper and lower continental crust. Chemical Geology, 276(3):188–197. **https://doi.org/10.1016/j.chemgeo.2010.06.005**

Winchester, J.A., and Floyd, P.A., 1977. Geochemical discrimination of different magma series and their differentiation products using immobile elements. Chemical Geology, 20:325–343. **https://doi.org/10.1016/0009-2541(77)90057-2**

Wood, D.A., 1980. The application of a ThHfTa diagram to problems of tectonomagmatic classification and to establishing the nature of crustal contamination of basaltic lavas of the British Tertiary Volcanic Province. Earth and Planetary Science Letters, 50(1):11–30. **https://doi.org/10.1016/0012-821X(80)90116-8**

Workman, R.K., and Hart, S.R., 2005. Major and trace element composition of the depleted MORB mantle (DMM). Earth and Planetary Science Letters, 231(1–2):53–72. **https://doi.org/10.1016/j.epsl.2004.12.005**

Yakovlev, P.V., Saal, A., Clark, M.K., Hong, C., Niemi, N.A., and Mallick, S., 2019. The geochemistry of Tibetan lavas: spatial and temporal relationships, tectonic links and geodynamic implications. Earth and Planetary Science Letters, 520:115–126. **https://doi.org/10.1016/j.epsl.2019.04.032**

Yan, Q., Shi, Xuefa, and Li, N., 2011. Oxygen and lead isotope characteristics of granitic rocks from the Nansha block (South China Sea): implications for their petrogenesis and tectonic affinity. Island Arc, 20(2):150–159. **https://doi.org/10.1111/j.1440-1738.2010.00754.x**

Yan, Q., Shi, X., and Castillo, P.R., 2014. The late Mesozoic–Cenozoic tectonic evolution of the South China Sea: a petrologic perspective. Journal of Asian Earth Sciences, 85:178–201. **https://doi.org/10.1016/j.jseaes.2014.02.005**

Yan, Q., Shi, X., Liu, J., Wang, K., and Bu, W., 2010. Petrology and geochemistry of Mesozoic granitic rocks from the Nansha micro-block, the South China Sea: constraints on the basement nature. Journal of Asian Earth Sciences, 37(2):130–139. **https://doi.org/10.1016/j.jseaes.2009.08.001**

Yan, Q., Shi, X., Wang, K., Bu, W., and Xiao, L., 2008. Major element, trace element, and Sr, Nd and Pb isotope studies of Cenozoic basalts from the South China Sea. Science in China Series D: Earth Sciences, 51(4):550–566. **https://doi.org/10.1007/s11430-008-0026-3**

Yan, Q., Straub, S., and Shi, X., 2019. Hafnium isotopic constraints on the origin of late Miocene to Pliocene seamount basalts from the South China Sea and its tectonic implications. Journal of Asian Earth Sciences, 171:162–168. **https://doi.org/10.1016/j.jseaes.2018.06.027**

Zhang, G.-L., Chen, L.-H., Jackson, M.G., and Hofmann, A.W., 2017. Evolution of carbonated melt to alkali basalt in the South China Sea. Nature Geoscience, 10(3):229–235. **https://doi.org/10.1038/ngeo2877**

Zhang, G.-L., Sun, W.-D., and Seward, G., 2018. Mantle source and magmatic evolution of the dying spreading ridge in the South China Sea. Geochemistry, Geophysics, Geosystems, 19(11):4385–4399. **https://doi.org/10.1029/2018GC007570**

Zhou, D., and Yao, B., 2009. Tectonics and sedimentary basins of the South China Sea: challenges and progresses. Journal of Earth Science, 20(1):1–12. **https://doi.org/10.1007/s12583-009-0001-8**